Superlattice structure of Ce^{3+}-doped BaMgF$_4$ fluoride crystals - x-ray diffraction, electron spin-resonance, and optical investigations

Superlattice structure of Ce^{3+}-doped $BaMgF_4$ fluoride crystals—x-ray diffraction, electron spin-resonance, and optical investigations

M Yamaga[1]**, K Hattori**[1]**, N Kodama**[2]**, N Ishizawa**[3]**, M Honda**[4]**, K Shimamura**[5] **and T Fukuda**[5]

[1] Department of Electrical and Electronic Engineering, Faculty of Engineering, Gifu University, Gifu, 501-1193, Japan
[2] Department of Materials Science and Engineering,
Faculty of Engineering and Resource Science, Akita University, Akita, 010-8502, Japan
[3] Materials and Structures Laboratory, Tokyo Institute of Technology, Yokohama, 226-8503, Japan
[4] Faculty of Science, Naruto University of Education, Naruto, 772-8502, Japan
[5] Institute for Materials Research, Tohoku University, Sendai, 980-8577, Japan

Abstract
The x-ray diffraction patterns for Ce^{3+}-doped $BaMgF_4$ (BMF) crystals suggest the existence of superlattice structure. The superlattice model is consistent with the characterization of the $4f^1$ ground state of Ce^{3+} as a probe ion using the electron spin-resonance (ESR) technique. The distinct Ce^{3+} luminescence spectra with different peak energies and lifetimes also support the superlattice model. Although the detailed superlattice structure could not be analysed using the diffraction spots, a model has been proposed, taking into account the eight Ce^{3+} polyhedra with different anion coordinations in the unit cell of the BMF crystal obtained from the ESR experiments.

1. Introduction

There is much interest in Ce^{3+}-doped ionic crystals in view of their applications in scintillators and tunable lasers [1, 2]. Recently, operations of optically pumped tunable solid-state lasers in the UV region using the 5d–4f transition of Ce^{3+} in the fluoride crystals $LiYF_4$ (LYF) [3] and $LiCaAlF_6$ (LiCAF) [4] were reported. In order to design systems to produce certain lasing frequencies, tuning ranges, and output powers, it is important to examine how the symmetry and strength of the crystal fields in Ce^{3+}-doped fluoride crystals determine the energy levels of the excited states, the electron–phonon coupling, and the radiative decay rate [5].

In a previous paper [6], we reported different optical spectra of Ce^{3+} in two kinds of $BaMgF_4$ (BMF) crystal grown by spontaneous crystallization from slowly cooled melts and

by the Czochralski technique. Although the optical spectra for both crystals are assigned as arising from optical transitions from unperturbed and perturbed Ce^{3+} ions, the origins of the Ce^{3+} centres in the two crystals are different because the peak energies of the optical spectra are different. In order to explain this fact, the unperturbed Ce^{3+} ions have been assumed to substitute selectively for two distinct ordinary cations—for example, Ba^{2+} and Mg^{2+}. However, this model is inappropriate because of the ionic size mismatch between Ce^{3+} and Mg^{2+}.

In order to resolve this problem, we have examined the crystal structure of BMF and the surroundings of the Ce^{3+} ions using the x-ray diffraction and electron spin-resonance (ESR) techniques, respectively. The x-ray diffraction suggests the existence of superlattice structure in the BMF crystal—that is, two or more Ba^{2+} ordinary sites with different local structures in a unit cell. This paper reports that the superlattice structure deduced from the x-ray diffraction is coincident with the characterization of the $4f^1$ ground state and $5d^1$ excited state of Ce^{3+} as a probe ion using the ESR and optical techniques.

2. Crystal structure and experimental procedure

The BMF crystal is reported to have orthorhombic structure with space group C_{2v}^{12} ($Cmc2_1$) [7]. The lattice constants are obtained as $a = 5.809$ Å, $b = 14.58$ Å, and $c = 4.126$ Å from the powder x-ray diffraction. The unit cell is shown in figure 1(a). Each octahedron consists of a central Mg^{2+} ion and six nearest-neighbour F^- ligand ions. Ba^{2+} ions are located at centres of trigonal prisms, each composed of six nearest-neighbour F^- ligand ions. Ba^{2+} ions are also surrounded by five F^- ions in the c-plane containing the Ba^{2+} ion (see figure 10 later). According to reference [7], the distances between Ba^{2+} and F^- ions (numbered 1 and 2 in figure 10), which are shorter than those between the remaining three ions (numbered 3, 4, and 5 in figure 10), are very close to those between Ba^{2+} and F^- ions in a trigonal prism. The directions from the Ba^{2+} ion to the nearest-neighbour F^- ligand ions are denoted by dashed lines in figure 1(a). Two distinct Ba(1) and Ba(2) sites are symmetric with respect to the b-plane. The positions of Ba(2) along the c-axis are shifted to $\pm c/2$ relative to those of Ba(1). Figure 1(b) shows a Ba^{2+} polyhedron, in which a back plane containing four F^- ions is roughly rotated from the cubic configuration by about $45°$, and that the axial distortion is approximately perpendicular to these planes. Ce^{3+} ions substitute preferentially for Ba^{2+} ions in the polyhedra with approximate C_{2v} symmetry, because the ionic radius (1.11 Å) of Ce^{3+} is larger than that (0.86 Å) of Mg^{2+} and smaller than that (1.56 Å) of Ba^{2+} [8].

Ce^{3+}-doped BMF crystals were grown in a vacuum-tight Czochralski system equipped with a graphite heater and automatic control of the boule diameter. The starting charges were formed from a stoichiometric mixture of BaF_2(50 mol%) and MgF_2(50 mol%). Two BMF crystals were codoped with 0.5 at.% Ce^{3+} ions and 0.5 (2.5) at.% Na^+ ions as charge compensators for Ba^{2+} ions. The compounds were melted and soaked in a furnace under a reactive atmosphere of CF_4. The crystals were grown along the crystalline a-axis at a pulling rate of 1 mm h^{-1} and a rotation rate of 15 rpm.

X-ray diffraction measured at 300 K was used to determine the crystal structure using the oscillation mode in the range $\pm60°$ for the Mo Kα_1 radiation (0.709 26 Å) with a Rigaku T-AXIS RAPID x-ray diffraction camera. Oriented samples were cut parallel to the crystalline a-, b-, and c-axes for ESR and optical measurements.

The ESR measurements of Ce^{3+} in BMF were made over the temperature range 5 to 100 K using a Bruker EMX10/12 X-band spectrometer with microwave frequencies of 9.686 to 9.698 GHz, microwave power of 1 mW, and 100 kHz field modulation. The angular variations of the ESR spectra were measured by rotating the sample in a cavity.
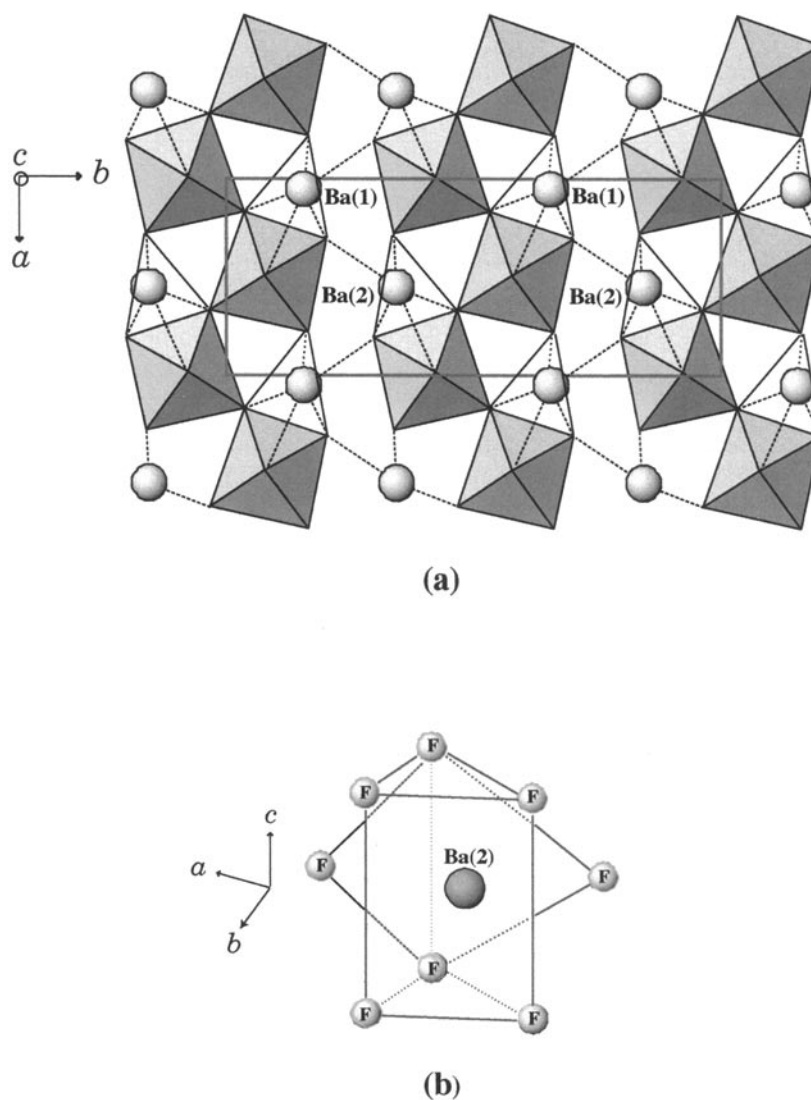
Figure 1. (a) A unit cell of the crystal structure of BaMgF$_4$ with the space group of C$_{2v}^{12}$. Each octahedron consists of a central Mg^{2+} ion and six nearest-neighbour F$^-$ ligand ions. Ba^{2+} ions are located at centres of trigonal prisms. The dotted lines emerging from the Ba denote directions of the nearest-neighbour F$^-$ ligand ions. Ba(1) and Ba(2) are symmetric with respect to the b-plane. (b) An eightfold-anion-coordination polyhedron of Ba(2), where one of two parallel planes in the cubic configuration is rotated by about 45°.

Optical absorption spectra were measured using a Hitachi U-3500 spectrophotometer at 300 K in the region 190–2500 nm. Polarized optical absorption was measured by placing a Glan–Taylor prism in a sample beam of the spectrophotometer in the wavelength range above 220 nm. Luminescence and excitation spectra were measured at 300 K using a Hitachi F-4500 fluorescence spectrophotometer. The lifetime of the Ce^{3+} luminescence was measured using a Horiba NAES-700F time-resolved photoluminescence spectrometer at 300 K at the Instrumental Analysis Centre, Gifu University.

3. Experimental results

3.1. X-ray diffraction

Figure 2 shows the x-ray oscillation photograph, taken for rotation around the crystalline c-axis, of BMF:Ce^{3+}(0.5%):Na^+(2.5%) at 300 K. The diffraction spots from reciprocal-lattice planes parallel to the a^*b^*-plane represent a typical superlattice structure pattern, which consists of strong main reflections and additional weak satellite reflections. The main reflections are caused by the basic structure with symmetry C_{2v}^{12} [7]. The weak satellite reflections are associated with the modulation structure. The satellite spots lie midway between two main-reflection-layer lines, so the satellites show the reciprocal-lattice vector $\frac{1}{2}c^*$. Although the same superlattice structure patterns for the b^*c^*- and c^*a^*-planes were observed, the satellite spots from the c^*a^*-plane were somewhat weak in intensity compared with those from the a^*b^*- and b^*c^*-planes. These results suggest commensurate superlattice structure with approximately twofold periodicity along the c- and a-axes.
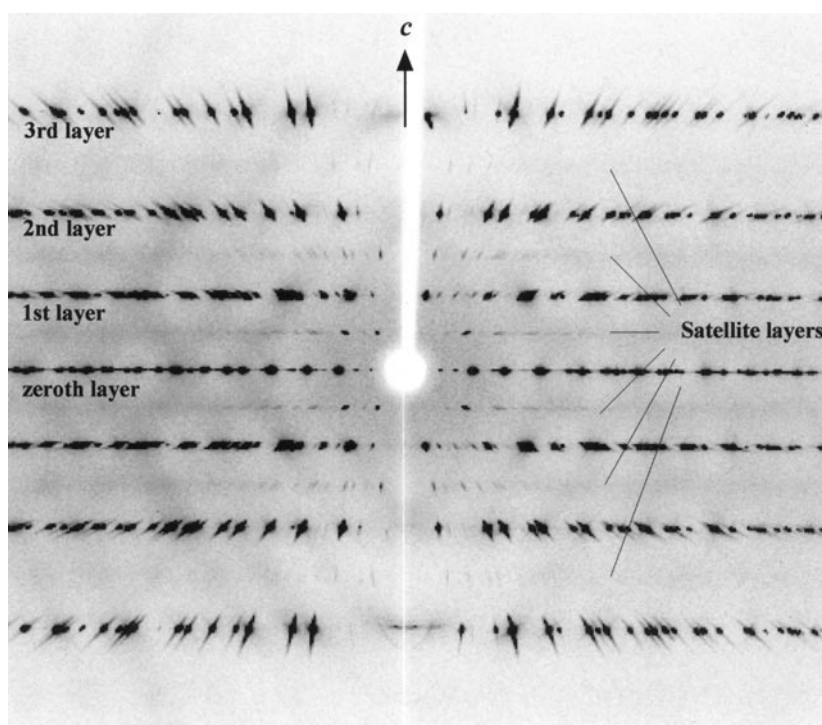

Figure 2. X-ray oscillation photographs of $BaMgF_4$:Ce^{3+}(0.5%):Na^+(2.5%) for rotations around the crystalline c-axis.

3.2. ESR spectra

Figure 3 shows the ESR spectra of BMF:Ce^{3+}(0.5%):Na^+(0.5%) measured over the temperature range 5–40 K with a microwave frequency of $\sim$9.690 GHz and magnetic field B parallel to the crystalline c-axis. The spectrum observed at 5 K consists of two resonance lines denoted by A and B. As temperatures increase, the A signal gradually decreases, whereas the B signal increases slightly, reaches a maximum at $\sim$10 K and decreases above $\sim$10 K. The widths of the
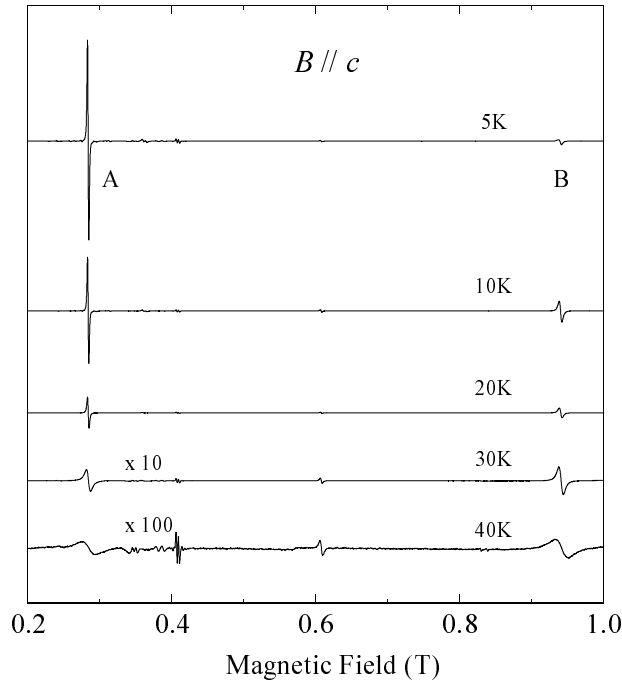
Figure 3. ESR spectra of BaMgF$_4$:Ce^{3+}(0.5%):Na$^+$(0.5%) measured in the temperature range 5–40 K with a microwave frequency of 9.690 GHz and $B \parallel c$. Ce^{3+} ESR signals are denoted by A and B. Signals in the range 0.35–0.41 T are due to impurities in the cavity.

A and B lines measured above 30 K are broadened and their integrated intensities are nearly equal to each other. The A and B lines are not observed above 50 K due to line broadening. The line at $B \sim 0.6$ T and $T = 40$ K is comparable with the A and B lines in peak-to-peak intensity, but the linewidth is narrower than those for A and B. The origin may be different from those of the A and B lines. In addition, sharp lines observed around 0.35–0.41 T in the temperature range 5–40 K are due to impurities in the cavity.

The ESR spectra are observed at 10 K for magnetic field rotations in the a-, b-, and c-planes. Figure 4 shows the angular variations of the g-values calculated using $h\nu = g\mu_B B S$ where h is the Planck constant, μ represents microwave frequencies of 9.686–9.698 GHz, μ_B is the Bohr magneton, B is a resonance magnetic field, and S $(=\frac{1}{2})$ is an effective spin for Ce^{3+} ions. The angular variation patterns of the A and B lines show orthorhombic symmetry. Although each of the A and B lines is slightly split into two lines in the a- and b-planes, it is substantially split into two lines in the c-plane. This result indicates that the A and B lines are due to two Ce^{3+} polyhedra with different local structures in a unit cell, consisting of two or more magnetically inequivalent configurations. The orientation dependences of the g-values in figure 4 are analysed using an effective Hamiltonian appropriate to orthorhombic symmetry [9, 10]:

$$\mathcal{H} = \mu_B g_x B_x S_x + \mu_B g_y B_y S_y + \mu_B g_z B_z S_z. \tag{1}$$

In order to define the principal x-, y-, and z-axes of the Ce^{3+} orthorhombic centres, the crystalline a-, b-, and c-axes are rotated around an arbitrary direction. This is achieved through a succession of three rotations: a first rotation by an angle ϕ about the c-axis, the new axes being a', b', and c' ($=c$); a second rotation by an angle θ about the b'-axis, the new axes being
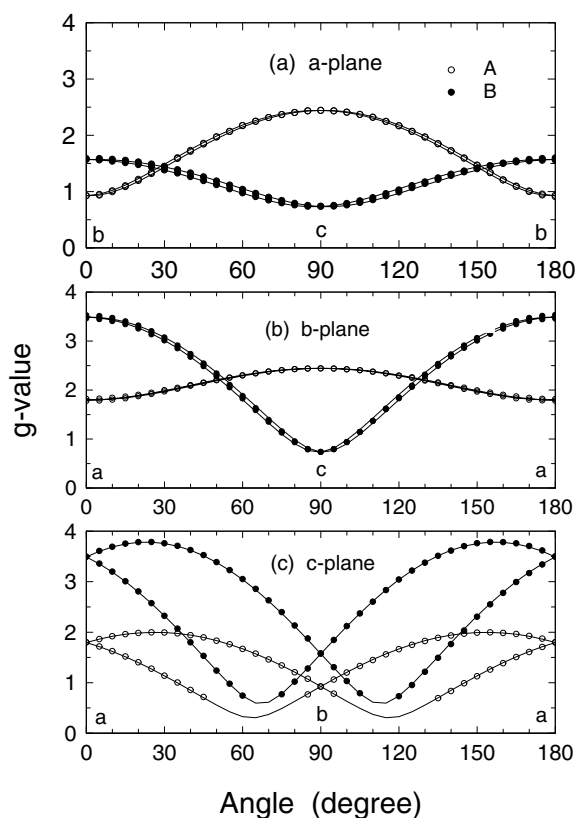
Figure 4. Angular variations of the *g*-values for BaMgF$_4$:Ce^{3+}(0.5%):Na$^+$(0.5%) at 10 K for magnetic field rotations in the *a*-, *b*-, and *c*-planes. The solid curves were calculated using equation (1) and the values in table 1.

Table 1. The spin-Hamiltonian parameters in equation (1) and the activation energy in equation (2) measured for Ce^{3+} ions in the BaMgF$_4$ crystal.

Centre	A			B		
g-values	$g_x = 1.997$	$g_y = 2.443$	$g_z = 0.299$	$g_x = 0.580$	$g_y = 0.731$	$g_z = 3.784$
	$\tilde{g} = 1.580$			$\tilde{g} = 1.698$		
Polar angles (deg)	$\theta = \pm 89$	$\phi = \pm 67$	$\psi = 0$	$\theta = \pm 89$	$\phi = \pm 26$	$\psi = 0$
ΔE (cm^{-1})	105			118		

a'', b'' ($=b'$), and c''; and a third rotation by an angle ψ about the c''-axis. The a'''-, b'''-, and c'''-axes are defined as the *x*-, *y*-, and *z*-axes corresponding to the *g*-tensor. The *z*-axis extent of the *g*-tensor as determined experimentally is found to be substantially different from the two other *g*-values. The full curves in figure 4, calculated using equation (1) with the *g*-values for A and B given in table 1, are in good agreement with the experimental points. The ESR results indicate that the *z*-axes for the A and B lines are approximately in the *c*-plane and normal to each other, and that each of them has four magnetically inequivalent configurations, which are reduced to two magnetically inequivalent configurations with magnetic fields applied in

the a-, b-, and c-planes. Such magnetically inequivalent configurations are seen in the ESR spectra in figure 5. The four ESR lines for A and B are observed with magnetic fields applied slightly away from the a- and c-axes by $\sim 2°$ and $\sim 5°$, respectively.
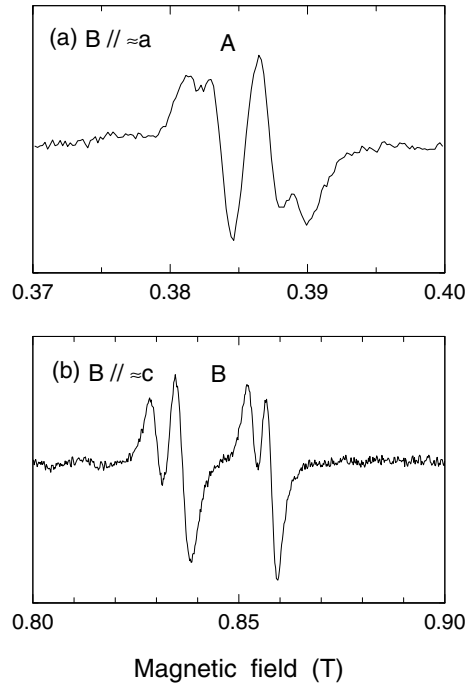

Figure 5. ESR spectra for A and B in BaMgF$_4$:Ce^{3+}(0.5%):Na$^+$(0.5%) observed with magnetic fields applied slightly away from the a- and c-axes by $\sim 2°$ and $\sim 5°$, respectively.

As shown in figure 3, the peak-to-peak intensities of the A and B lines decrease and the linewidths are broadened with increasing temperature. Such temperature dependence is caused by spin–lattice relaxation rates enhanced at high temperatures. Direct, Raman, and Orbach processes lead to increase of the homogeneous linewidth. The direct process may be discounted since the observed broadening, beyond detection, is much too fast for this effect. The width of the ESR line with $B \parallel c$, which is equal to the peak-to-peak separation of the differential curve, is plotted in figure 6 as a function of inverse temperature. The temperature dependence of the linewidth is calculated to be of the form [9, 10]

$$\Gamma = a + bT^9 + c\exp(-\Delta E/kT). \tag{2}$$

The first term represents the temperature-independent inhomogeneous broadening, which is induced by random strains in the crystal. The second and third terms are associated with the Raman and Orbach processes with the thermal activation energy ΔE, respectively. The values of the fitting parameter ΔE for the A and B lines are also summarized in table 1. The activation energy is given by the energy separation between the ground and first excited states of Ce^{3+}, which is determined by the crystal-field interaction. As the activation energies are nearly equal to each other, the strength of the orthorhombic distortion is expected to be very similar.

Although the ESR spectrum measured with $B \parallel c$ for BMF:Ce^{3+}(0.5%):Na$^+$(2.5%) did not change in shape, the widths of the A and B lines were enhanced to about 1.6 and 2.3 times larger than those for BMF:Ce^{3+}(0.5%):Na$^+$(0.5%). In addition, satellite lines around the A line
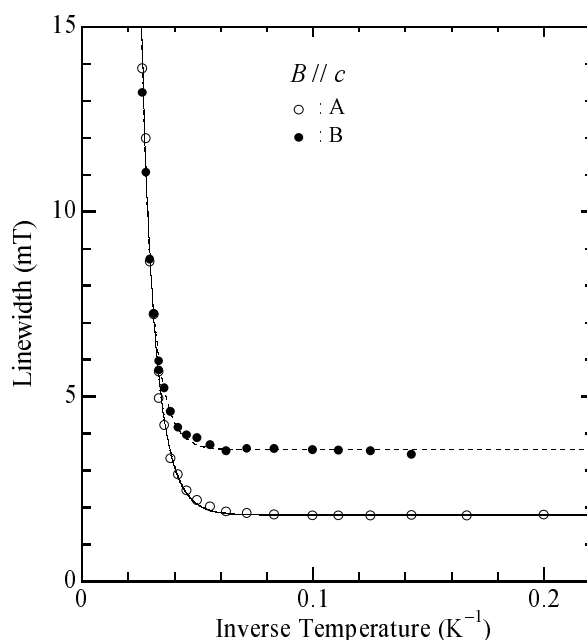
Figure 6. Widths (mT) of the ESR lines for $BaMgF_4:Ce^{3+}(0.5\%):Na^+(0.5\%)$ with $B \parallel c$ which are equal to the peak-to-peak separation of the resonance as a function of inverse temperature. The solid and dashed curves for A and B, respectively, are calculated using equation (2).

at 0.283 T were observed. As the angular variations of the satellite lines were very complicated, exact g-value analyses could not be carried out. These results suggest that strains created by Na^+ near to Ce^{3+} enhance the widths of the A and B lines and that Na^+ substitutions for the nearest-neighbour Ba^{2+} ions, as charge compensators, strongly perturb the Ce^{3+} polyhedra. In consequence, the A and B lines are due to the Ce^{3+} polyhedra, being less perturbed by Na^+ charge compensators away from Ce^{3+}.

3.3. Optical spectra

Figure 7 shows the unpolarized and polarized optical absorption spectra of $BMF:Ce^{3+}(0.5\%):Na^+(0.5\%)$. The polarized spectrum shows clearly an intense band with a peak at 248 nm in addition to the four intense bands at 200, 218, 231, and 259 nm observed in the unpolarized absorption spectrum. The five bands are assigned as due to the optical transitions from the $4f^1$ ground state to the five Kramers doublets of the $5d^1$ excited state of Ce^{3+} occupying ordinary sites in the BMF crystals [6]. An additional weak band observed at $\sim$300 nm is enhanced for $BMF:Ce^{3+}(0.5\%):Na^+(2.5\%)$. The 300 nm band is due to the Ce^{3+} centres perturbed by charge compensators—for example, Na^+ ions or cation vacancies [6].

UV excitation in the range 220–300 nm for $BMF:Ce^{3+}(0.5\%):Na^+(0.5\%)$ produces a broad luminescence band with a peak at $\sim$300 nm as shown in figure 8(a). The luminescence spectra excited in the range 220–270 nm consist of two broad bands denoted by A_1 and A_2, whereas two broad bands denoted by B_1 and B_2 observed with excitation wavelengths of 275–280 nm are slightly shifted to lower energy. Other broad bands denoted by C_1 and C_2 appear at wavelengths $\lambda_{ex} > 280$ nm and are somewhat shifted to lower energy. The Ce^{3+} spectrum of luminescence from a single Ce^{3+} site should be decomposed into two Gaussians with the energy separation
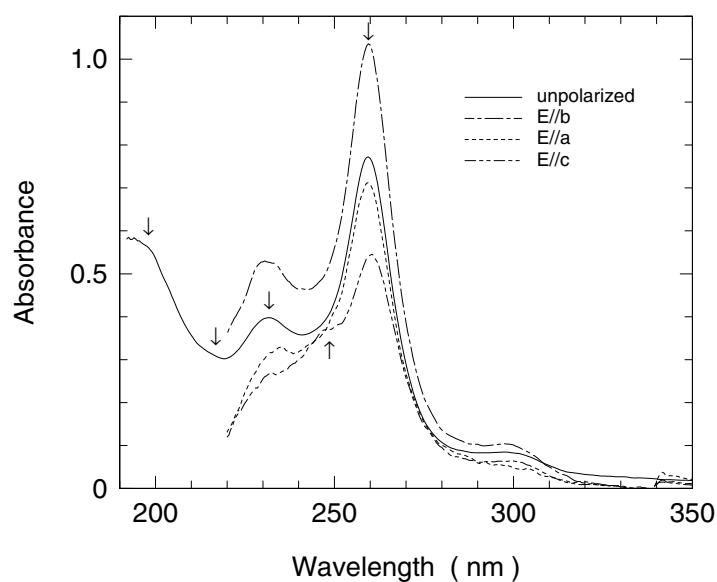
Figure 7. Unpolarized and polarized optical absorption spectra of BaMgF$_4$:Ce^{3+}(0.5%): Na$^+$(0.5%). Arrows indicate peak positions.

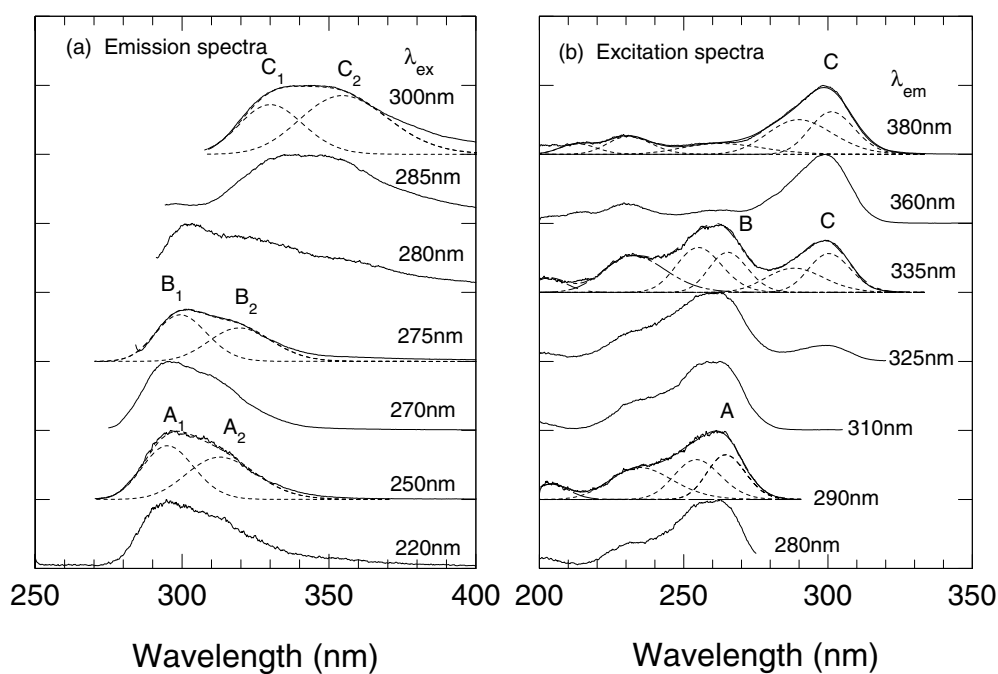**Figure 8.** (a) Luminescence spectra of BaMgF$_4$:Ce^{3+}(0.5%):Na$^+$(0.5%) excited with different wavelengths. The luminescence spectra excited at 250, 275, and 300 nm are deconvoluted into two Gaussians denoted by (A$_1$, A$_2$), (B$_1$, B$_2$), and (C$_1$, C$_2$). (b) Excitation spectra of the Ce^{3+} luminescence at different fixed wavelengths. The excitation bands denoted by A, B, and C correspond to the (A$_1$, A$_2$), (B$_1$, B$_2$), and (C$_1$, C$_2$) luminescence bands, respectively.

2200 cm^{-1}, which is equal to the ground-state splitting between $^2F_{5/2}$ and $^2F_{7/2}$ of Ce^{3+}. The dashed curves in figure 8(a) represent two Gaussians calculated through fitting the observed spectra to the energy scale. The observed energy separations for the A$_1$/A$_2$, B$_1$/B$_2$, and C$_1$/C$_2$ bands are ∼2100, 2050, and 2100 cm^{-1}, respectively.

The excitation spectra of the luminescence in BMF:Ce^{3+}(0.5%):Na$^+$(0.5%) were measured over the wavelength range 280–380 nm as shown in figure 8(b). The excitation spectra with $\lambda_{em} < 310$ nm are similar to the unpolarized absorption spectrum in figure 7. The line shapes change drastically above $\lambda_{em} \sim 310$ nm; that is, the 300 nm bands denoted by C are enhanced. In order to estimate the peak energy of the bands, the spectra with $\lambda_{em} = 290$, 335, and 380 nm are deconvoluted into several Gaussians in figure 8(b). The C excitation spectrum with $\lambda_{em} \sim 380$ nm shows five distinct bands corresponding to the five 5d^1 excited states of Ce^{3+}. The clear peak shift of the B excitation spectrum to lower energy is not observed.

Figure 9 shows the lifetimes of the luminescence excited at 260, 270, and 300 nm and the intensities integrated in a time domain as a function of the luminescence wavelength. The lifetimes with $\lambda_{ex} = 260$ nm are obtained as the constant values 25 and 50 ns in the wavelength ranges 280–320 nm and 350–400 nm, respectively, corresponding to the A$_1$/A$_2$ broad band and the tail to longer wavelength. In the case of $\lambda_{ex} = 270$ nm, the lifetimes are constant (25 ns) below $\lambda_{em} \sim 300$ nm, and show an increase in the form of a small step around $\lambda_{em} \sim 330$ nm. The intensity spectrum with $\lambda_{ex} = 270$ nm is shifted to longer wavelength
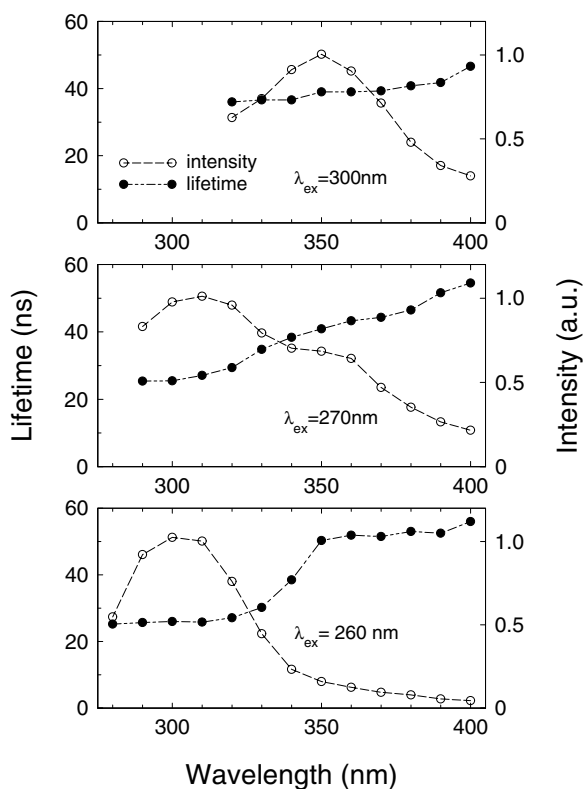

Figure 9. Lifetimes of the luminescence excited at 260, 270, and 300 nm and intensities integrated in a time domain as a function of the luminescence wavelength measured at 300 K for BaMgF$_4$:Ce^{3+}(0.5%):Na$^+$(0.5%).

by $\sim$10 nm compared with that with $\lambda_{ex} = 260$ nm. The line shape is similar to that of the B$_1$/B$_2$ luminescence spectrum excited at 280 nm in figure 8(a). The lifetime ($\sim$30 ns) at $\lambda_{em} = 310$ nm with the peak intensity, which is attributed to the B$_1$/B$_2$ luminescence band, is slightly larger than that (25 ns) of the A$_1$/A$_2$ luminescence bands. The lifetimes of the C$_1$/C$_2$ luminescence bands excited at $\lambda_{ex} = 300$ nm are $\sim$40 ns, and gradually increase with increase of the wavelength. Although the C$_1$/C$_2$ luminescence bands excited at $\lambda_{ex} = 270$ and 300 nm and the tail (50 ns) excited at $\lambda_{ex} = 260$ nm are due to perturbed Ce^{3+} centres, they may be associated with different charge compensations.

4. Discussion

4.1. g-value

The observed g-values, $(g_x, g_y, g_z) = (1.997, 2.443, 0.299)$ and $(0.580, 0.731, 3.784)$ for A and B, show orthorhombic symmetry. The mean g-values, $\tilde{g} = \frac{1}{3}(g_x + g_y + g_z)$ for A and B, are 1.580 and 1.698. The result that they are less than 2 and larger than 10/7 indicates that for A and B, Ce^{3+} ions substitute for Ba^{2+} ions with an eightfold coordination [11, 12].

First, we discuss the g-values on the assumption that these Ce^{3+} centres can be approximated as being tetragonal. The approximate values $g_\parallel = g_z$ and $g_\perp = \frac{1}{2}(g_x + g_y)$ for A and B are set to $(g_\parallel, g_\perp) = (0.299, 2.220)$ and $(3.784, 0.656)$, respectively. The approximate g-values for A are in agreement with those, $(g_\parallel, g_\perp) = (0.299, 2.220)$, calculated using eigenfunctions of [13, 14]

$$\left| \frac{5}{2}, \pm\frac{1'}{2} \right\rangle = 0.953 \left| \frac{5}{2}, \pm\frac{1}{2} \right\rangle - 0.295 \left| \frac{7}{2}, \pm\frac{1}{2} \right\rangle + 0.054 \left| \frac{7}{2}, \mp\frac{7}{2} \right\rangle \tag{3}$$

where mixing between $|\frac{5}{2}, \pm\frac{1}{2}\rangle$ and $(|\frac{7}{2}, \pm\frac{1}{2}\rangle, |\frac{7}{2}, \mp\frac{7}{2}\rangle)$ occurs through the second-order perturbation of the axial crystal-field interaction and the spin–orbit interaction. On the other hand, the g-values for B are close to those, $(g_\parallel, g_\perp) = (30/7, 0)$, calculated for $|\frac{5}{2}, \pm\frac{5}{2}\rangle$.

The difference in g_x and g_y between A and B is induced by an orthorhombic distortion represented by the spin operator $B_2^2 O_2^2$ [9]. The eigenfunction of the Hamiltonian of the crystal-field interaction including an orthorhombic distortion is given in the form

$$\left| \pm\frac{\tilde{1}}{2} \right\rangle = p \left| \frac{5}{2}, \pm\frac{1}{2} \right\rangle + q \left| \frac{5}{2}, \pm\frac{5}{2} \right\rangle + r \left| \frac{5}{2}, \mp\frac{3}{2} \right\rangle \tag{4}$$

where $p^2 + q^2 + r^2 = 1$. The formula for the g-values calculated using equation (4) was given by McLaughlan and Forrester [15]. The observed g-values for B in table 1 are very close to those, $(g_x, g_y, g_z) = (0.522, 0.88, 3.87)$, calculated using the g-value formula [15] and parameters $(p, q, r) = (-0.175, 0.962, -0.211)$ in equation (4). The small difference between the observed and calculated g-values can be removed by mixing the $^2F_{7/2}$ excited state into the $^2F_{5/2}$ ground state through the second-order perturbation [14]. The g-values for A are calculated using equation (4), replacing $|\frac{5}{2}, \pm\frac{1}{2}\rangle$ with $|\frac{5}{2}, \pm\frac{1'}{2}\rangle$ of equation (3). The values $(g_x, g_y, g_z) = (1.997, 2.441, 0.299)$ calculated using the parameters $(p, q, r) = (0.998, -0.039, -0.0469)$ are in good agreement with the observed g-values given in table 1 because the $^2F_{7/2}$ excited state was already included.

The remarkable ESR results for Ce^{3+} are as follows:

(i) Ce^{3+} ions substitute for two distinct Ba^{2+} polyhedra with an eightfold coordination in the BMF crystal and each of them has four magnetically inequivalent configurations. In total, there are eight different Ce^{3+} polyhedra in a unit cell, as shown in figure 5.

(ii) The integrated intensities of the A and B lines measured at 40 K in figure 3 are the same. The populations of the eight Ce^{3+} polyhedra in the BMF crystal are equal to each other.

(iii) The A and B polyhedra are elongated and compressed because the dominant components of their eigenfunctions are equal to $|\frac{5}{2}, \pm\frac{1}{2}\rangle$ and $|\frac{5}{2}, \pm\frac{5}{2}\rangle$, respectively. The principal z-axes of the distorted polyhedra are approximately normal to each other.

4.2. Optical spectra

The ^2D excited state of the Ce^{3+} polyhedron with symmetry C_{2v} in BMF is split into five Kramers doublets, corresponding to the five main overlapping absorption bands at 200, 218, 231, 248, and 259 nm in figure 7. The 300 nm absorption band is shifted to lower energy and enhanced with increase of the Na^+ concentration. It is assigned as due to Ce^{3+} ions perturbed by charge compensators—for example, Na^+ ions and/or cation vacancies [6].

We focus on discussing the relation between the superlattice structure and the optical properties of Ce^{3+} in BMF—for example, the A_1/A_2 and B_1/B_2 luminescence bands and their lifetimes. The peak energies and lifetimes of the A_1 and B_1 luminescence bands are (34 200, 33 400 cm^{-1}) and (25, 30 ns), respectively. The energy levels of the $5d^1$ excited state of the Ce^{3+} polyhedra are slightly modified by low-symmetry components of distortions. As the symmetry of the polyhedra is reduced, the energy of the lowest excited state is shifted to lower energy and the 5d–4f optical transition probabilities are also reduced [16]. In consequence, the low-symmetry components produced by the superlattice structure are expected to modify the energy levels of Ce^{3+}.

4.3. Superlattice structure

Although the x-ray diffraction in figure 2 indicates superlattice structure, we could not obtain the exact structure of the Ba^{2+} polyhedra using the x-ray diffraction data because of there being fewer data points. Here we propose a superlattice model for the BMF crystal, taking account of the above ESR results.

The C_{2v}^{12} crystal structure of BMF is shown in figure 1(a). There are two Ba(1) and Ba(2) sites, which are symmetric with respect to the b-plane. When Ce^{3+} ions substitute for Ba(1) and Ba(2) ions, they cannot be distinguished from the energy levels of Ce^{3+}—for example, in optical absorption spectra. This means that Ba(1) and Ba(2) sites are structurally equivalent. On the other hand, when a magnetic field is applied to any direction of the crystal, Ba(1) and Ba(2) sites can be distinguished from different g-values. They are magnetically inequivalent.

The ESR results that eight structurally and magnetically inequivalent Ce^{3+} polyhedra exist in the BMF crystal are inconsistent with the C_{2v}^{12} crystal structure as discussed above. This discrepancy can be removed by using a superlattice model. The superlattice structure obtained from the x-ray diffraction possesses approximately twofold periodicity along the a- and c-axes; that is, the unit cell is four times larger than that of the C_{2v}^{12} crystal structure, resulting in 2×4 different Ba sites. This prediction is consistent with the ESR results.

Figure 10 shows the projection of a Ba^{2+} polyhedron on the c-plane, where five F(i) ($i = 1-5$) ligand ions are located in the same plane, also including the Ba^{2+} ion. If F(1)/F(2) and/or F(3)/F(4) ligand ions are displaced towards arrows in figure 10(a), the polyhedra are expected to be elongated or compressed along the directions of the arrows. Figure 10(b) shows the other distortion, which is approximately normal to that in figure 10(a). The angles between the distortion axis and the a-axis in figures 10(a) and 10(b) are ~60° and ~20°, respectively. These angles are close to the angle, ϕ, between the a-axis and the principal z-axes for A and
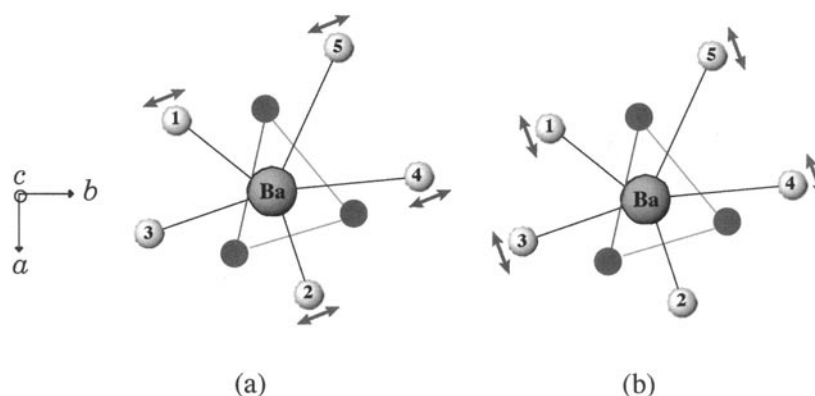
Figure 10. The projection of Ce^{3+} polyhedra along the c-plane with different displacements of F$^-$ ligand ions. Three solid circles represent a trigonal prism. F$^-$ ligand ions denoted by shadow circles numbered 1–5 are in the c-pane including a Ba^{2+} ion. Arrows denote directions of distortions.

B in table 1. In addition, four magnetically inequivalent sites may be created by symmetry operations with respect to the a- and c-planes.

5. Conclusions

The x-ray diffraction patterns for the BMF crystals indicate the existence of superlattice structure. The ESR and optical results for Ce^{3+} as a probe ion support the superlattice structure. Although the detailed superlattice structure could not be analysed using the diffraction spots, a superlattice model has been proposed, taking into account the eight structurally and magnetically inequivalent Ce^{3+} polyhedra in the BMF crystal obtained from the ESR results.

Acknowledgments

References

[1] Moulton P F 1985 *Laser Handbook* vol 5, ed M Bass and M H Stitch (Amsterdam: North-Holland) p 282
[2] Blasse G and Grabmaier B C 1994 *Luminescent Materials* (Berlin: Springer)
[3] Ehrlich T D J, Moulton P F and Osgood R M 1978 *Opt. Lett.* **4** 184
[4] Marshall C D, Speth J A, Payne S A, Krupke W F, Quarles G J, Castillo V and Chai B T H 1994 *J. Opt. Soc. Am.* B **11** 2054
[5] Kodama N, Yamaga M and Henderson B 1998 *J. Appl. Phys.* **84** 5820
[6] Yamaga M, Imai T and Kodama N 2000 *J. Lumin.* **87–89** 992
[7] Keve E T, Abrahams S C and Bernstein J L 1969 *J. Chem. Phys.* **51** 4928
[8] Kaminskii A A 1990 *Laser Crystals* (Berlin: Springer) table 2.1
[9] Abragam A and Bleaney B 1970 *Electron Paramagnetic Resonance of Transition Ions* (Oxford: Clarendon)
[10] Pibrow J R 1990 *Transition Ion Electron Paramagnetic Resonance* (Oxford: Clarendon)
[11] Rubins R S 1970 *Phys. Rev.* B **1** 139
[12] Ibragimov I R, Fazlizhanov I I, Falin M L and Ulanov V A 1992 *Fiz. Tverd. Tela* **34** 3261 (Engl. Transl. 1992 *Sov. Phys.–Solid State* **34** 1745)

[13] Elliott R J and Stevens K W H 1952 *Proc. R. Soc.* A **215** 437
[14] Yamaga M, Honda M, Shimamura K, Fukuda T and Yosida T 2000 *J. Phys.: Condens. Matter* **12** 5917
[15] McLaughlan S D and Forrester P A 1966 *Phys. Rev.* **151** 311
[16] Yamaga M, Imai T, Miyairi H and Kodama N 2001 *J. Phys.: Condens. Matter* **13** 753